JOURNAL OF GEOPHYSICAL RESEARCH, VOL. 115, E05001, doi:10.1029/2009JE003472, 2010

Click Here for Full Article

# GLGM-3: A degree-150 lunar gravity model from the historical tracking data of NASA Moon orbiters

E. Mazarico,[1] F. G. Lemoine,[1] Shin-Chan Han,[1,2] and D. E. Smith[1,3]

Received 17 July 2009; revised 24 November 2009; accepted 17 December 2009; published 11 May 2010.

[1] In preparation for the radio science experiment of the Lunar Reconnaissance Orbiter (LRO) mission, we analyzed the available radio tracking data of previous NASA lunar orbiters. Our goal was to use these historical observations in combination with the new low-altitude data to be obtained by LRO. We performed Precision Orbit Determination on trajectory arcs from Lunar Orbiter 1 in 1966 to Lunar Prospector in 1998, using the GEODYN II program developed at NASA Goddard Space Flight Center. We then created a set of normal equations and solved for the coefficients of a spherical harmonics expansion of the lunar gravity potential up to degree and order 150. The GLGM-3 solution obtained with a global Kaula constraint ($2.5 \times 10^{-4} l^{-2}$) shows good agreement with model LP150Q from the Jet Propulsion Laboratory, especially over the nearside. The levels of data fit with both gravity models are very similar (Doppler RMS of ~0.2 and ~1–2 mm/s in the nominal and extended phases, respectively). Orbit overlaps and uncertainties estimated from the covariance matrix also agree well. GLGM-3 shows better correlation with lunar topography and admittance over the nearside at high degrees of expansion ($l > 100$), particularly near the poles. We also present three companion solutions, obtained with the same data set but using alternate inversion strategies that modify the power law constraint and expectation of the individual spherical harmonics coefficients. We give a detailed discussion of the performance of this family of gravity field solutions in terms of observation fit, orbit quality, and geophysical consistency.

**Citation:** Mazarico, E., F. G. Lemoine, S.-C. Han, and D. E. Smith (2010), GLGM-3: A degree-150 lunar gravity model from the historical tracking data of NASA Moon orbiters, *J. Geophys. Res.*, *115*, E05001, doi:10.1029/2009JE003472.

## 1. Introduction

### 1.1. Rationale

[2] The Lunar Reconnaissance Orbiter (LRO) mission marks the robotic return of NASA to the Moon. With the purpose of building high-resolution data sets to ultimately enable the landing of astronauts, the LRO spacecraft carries a suite of capable instruments, with a particular focus on the lunar poles, for determining high-resolution imagery, altimetry, surface thermal properties; mapping permanently shadowed regions and potential ice deposits within; and so forth [*Chin et al.*, 2007]. The S-band telecom subsystem will be used to track the spacecraft and precisely estimate its trajectory, which will allow the measurements of all the instruments to be precisely geolocated. When combined with the topographic data obtained by the laser altimeter (the Lunar Orbiter Laser Altimeter (LOLA); see *Smith et al.* [2009]), the radio tracking data will help define a new geodetic reference frame for the Moon. The required position knowledge (50 m total position; 1 m radial) is challenging, given the low altitude of the polar orbit [*Chin et al.*, 2007], and will necessitate new solutions of the lunar gravity field in order to model short-wavelength gravity anomalies not necessarily captured by current solutions.

[3] One of the largest perturbations on the LRO orbit will be errors in the knowledge of the lunar gravity field [*Lemoine et al.*, 2008; *Rowlands et al.*, 2009]. To reduce this error in spacecraft ephemerides, and in the mission data products, we have planned to create a tuned gravity model that merges the historical data (from Lunar Prospector, Clementine, the Apollo subsatellites, and the Lunar Orbiters 1–5) with the tracking data we will obtain from LRO, including the radiometric tracking data, the one-way laser data, and the LOLA-derived altimeter crossovers. We have reprocessed all the historical data [*Lemoine et al.*, 1997] with updated force models and planetary ephemerides (section 2.1). The data from the extended phase of the Lunar Prospector mission are especially valuable; this orbit (altitude 30 ± 15 km) is very similar to LRO's mapping orbit (polar, near-circular, altitude 50 ± 15 km), and we discuss the contribution of each in section 2.2. We also note the close similarity between the orbits of LRO and of the Lunar Prospector extended mission. The LRO mission will use

[1]NASA Goddard Space Flight Center, Greenbelt, Maryland, USA.
[2]Also at Goddard Earth Sciences and Technology Center, University of Maryland, Baltimore County, Baltimore, Maryland, USA.
[3]Also at Department of Earth, Atmospheric and Planetary Sciences, Massachusetts Institute of Technology, Cambridge, Massachusetts, USA.

Copyright 2010 by the American Geophysical Union.
0148-0227/10/2009JE003472

S-band tracking from the Universal Space Network rather than the Deep Space Network, in addition to precise one-way laser ranging and altimeter data in the form of crossovers for orbit determination. The Lunar Prospector data, because of their precision and coverage, will still form the cornerstone of any lunar geopotential models in the near term, even when LRO data are eventually analyzed and included. We expect the new LRO data will contribute incrementally by refining the low-degree field and by improving the determination of low-order *m*-daily harmonics [*Kaula*, 1966] and some of the zonal harmonics.

[4] Herein we summarize the results of our new high-resolution gravity field model from the historical data, GLGM-3, in the same line as *Goossens et al.* [2006] did before the JAXA SELENE mission.

### 1.2. Previous Work

[5] Lunar space geodesy has long been a challenge, owing to the tidal lock of the Moon with Earth that prevents simple orbiter missions from being tracked over a large part of its surface (typically ~40%, on the farside, for a 100 km altitude orbit). Effectively, this lack of radio tracking data has translated into a poor spatial resolution of the farside gravity, constrained only by the observation of the effect of the gravity field-induced perturbation on the spacecraft trajectory. Until recently, the best lunar gravity fields presented a clear contrast in predicted error between the two hemispheres. LP150Q (see A. S. Konopliv and the Lunar Prospector Gravity Science Team, LP150Q Spherical Harmonic Model, 2000, available at http://pds-geosciences.wustl.edu/lunar01/lp-l-rss-5-gravity-v1/lp_1001/sha/jgl150q1.sha, hereinafter referred to as Gravity Science Team, 2000), and the latest model from the Jet Propulsion Laboratory (JPL), in the family as LP165P described by *Konopliv et al.* [2001]. It combined data from all existing NASA orbiter missions, including the Lunar Prospector missions (1998–1999), and described several large-scale anomalies in the farside low-latitude region, thanks to the combination of data from satellites at various inclinations.

[6] The Japanese SELENE mission avoided this "farside data gap" problem by having a small satellite (in a high eccentric orbit) relay radio signals between ground stations and the main orbiter Kaguya when it was over the farside. These four-way tracking data were used to create the SGM90d solution [*Namiki et al.*, 2009], which revealed signatures of new gravity anomalies. Nevertheless, given Kaguya's 100 km orbit during its primary mission, the short-wavelengths anomalies that will affect the LRO orbit were not captured in SGM90d. Current orbit tests with the Lunar Prospector extended mission tracking data show that LP150Q may still provide better orbit performance for LRO.

### 1.3. Overview

[7] In section 2 we present the orbit determination method and the data processing strategy we used. We then detail how normal equations were created from the radio tracking data and how the gravity field was inverted. In section 3 we conduct a detailed analysis of the GLGM-3 solution. After a direct comparison with LP150Q, we assess the gravitational uncertainties and orbit performance, using data fit and prediction capability criteria. Geophysical performance, based on correlation and admittance calculations, is also addressed. Finally, before concluding the paper, we derive a family of alternate gravity field solutions resulting from experimenting with the power law constraint and a priori information. This allows us to study the variability of the solutions depending on the inversion approach used.

## 2. Gravity Field Solution

### 2.1. Method

[8] We use Precision Orbit Determination (POD) to estimate the gravity field of the Moon, similar to many studies in the past [e.g., *Konopliv et al.*, 1993, 2001; *Lemoine et al.*, 1997]. The gravitational anomalies are inferred from their impact on the spacecraft orbit, as observed by the tracking data. The measurements, which consist of S-band radiometric tracking data, are processed with a least squares orbit determination batch filter [*Kaula*, 1966; *Lawson and Hanson*, 1974; *Tapley et al.*, 2004]. Principally because of the buildup of force model error, the data arcs are usually no longer than 2 days. The normal equations are created by the NASA Goddard Space Flight Center Orbit Determination and Geodetic Parameter Estimation Program, GEODYN [*Pavlis et al.*, 2006]. The normal equations are aggregated by satellite and mission phase, and the gravity solutions are generated by using the companion SOLVE program [*McCarthy*, 2008]. The lunar potential is modeled by using spherical harmonics as in

$$V = \frac{GM}{r}\sum_{l=0}^{l_{\max}}\left(\frac{a_e}{r}\right)^l\sum_{m=0}^{l}\overline{P}_{lm}(\sin\varphi)\left[\overline{C}_{lm}\cos(m\lambda)+\overline{S}_{lm}\sin(m\lambda)\right] \tag{1}$$

where the expansion truncated at degree $l_{\max}$ is defined in terms of radius $r$, latitude $\varphi$, and longitude $\lambda$; $\overline{C}_{lm}$ and $\overline{S}_{lm}$ represent the normalized geopotential coefficients; $\overline{P}_{lm}$ is the normalized associated Legendre functions of degree $l$ and order $m$; $a_e$ is the reference equatorial radius of the Moon; and $GM$ is the gravitational constant of the Moon [*Kaula*, 1966]. The a priori lunar gravity model for this study was the degree-100 model LP100K [*Konopliv et al.*, 2001], which we used to speed up the orbit tests and evaluations. Because we adjust the coefficients to degree and order 150, we can make an assessment as to how the results of the current analysis agree with the LP150Q solution, also a degree-150 gravity field.

[9] The current analysis used the JPL DE421 ephemerides [*Williams et al.*, 2008], with the new lunar orientation parameters derived from recent lunar laser ranging data [*Seidelmann et al.*, 2002]. This means the lunar body-fixed coordinate system associated with any gravity model we derive will be based on the lunar orientation constants embedded in DE421. A new representation of the planetary radiation pressure for the Moon was applied. Cylindrical grids of the albedo and thermal emissions used were based on temperature data provided by D. Paige (personal communication, 2008). This contrasts with previous analyses [e.g., *Lemoine et al.*, 1997; *Goossens et al.*, 2006; *Goossens and Matsumoto*, 2008], in which a spherical harmonic was used to represent the planetary radiation pressure perturbation [*Floberghagen et al.*, 1999]. The albedo and thermal maps, uniformly spaced in cylindrical coordinates, are bili-

**Table 1.** Characteristics of the Historical Lunar Missions

| Mission | Start | End | Number of Arcs | Data Points (Doppler) | Periapsis (km) | Apoapsis (km) |
|---|---|---|---|---|---|---|
| Lunar Orbiter 1 | 08/10/66 | 10/28/66 | 70 | 48,575 | 50 | 1830 |
| Lunar Orbiter 2 | 11/10/66 | 07/24/67 | 90 | 77,726 | 50 | 1870 |
| Lunar Orbiter 3 | 02/09/67 | 10/06/67 | 73 | 62,264 | 50 | 1820/320 |
| Lunar Orbiter 4 | 05/08/67 | 07/10/67 | 32 | 48,688 | 2700/75 | 6000/4000 |
| Lunar Orbiter 5 | 08/05/67 | 01/29/68 | 70 | 42,916 | 100/170 | 1750/2000 |
| Apollo 15 subsatellite | 08/29/71 | 05/19/72 | 93 | 52,500 | 75 | 160 |
| Apollo 16 subsatellite | 04/27/72 | 05/29/72 | 46 | 42,579 | 30 | 190 |
| Clementine | 02/19/94 | 05/04/94 | 40 | 378,022 | 370 | 2960 |
| Lunar Prospector (nominal) | 01/11/98 | 12/18/98 | 184 | 2,198,751 | 90 | 110 |
| Lunar Prospector (extended) | 12/19/98 | 07/30/99 | 127 | 1,372,150 | 25 | 45 |

nearly interpolated at the evaluation points (of a ring model; see *Knocke* [1989] and *Knocke et al.* [1988]) instead of being calculated from the spherical harmonics expansion.

[10] To model the lunar solid tide, we use a Love Number $k_2$ of 0.027 [*Williams et al.*, 1987]. Other force and measurement modeling is similar to that described by *Lemoine et al.* [1997, p. 16,343], except that we apply updated models of ocean loading for the terrestrial tracking data sites, on the basis of the GOT00 ocean tide model [*Ray*, 1999] and an updated Earth orientation series supplied by the International Earth Rotation Service [*Dick and Richter*, 2008]. Weather data for the Deep Space Network complexes (supplied by Mars Global Surveyor and used by *Lemoine et al.* [2001]) were used to compute a troposphere correction for the Lunar Prospector tracking data. We made some attempts to locate geodetic survey reports or other station coordinate information for the Manned Space Flight Network stations but had no success and so did not readjust station coordinates in the current analysis. Station coordinate error may still be a factor in the Apollo subsatellite POD results.

[11] In addition to the initial state of the spacecraft, we adjusted scale factors for the solar radiation acceleration and for biases for the range and three-way Doppler measurements. Biases for the Lunar Prospector Doppler data existed because of the rotation of the spacecraft. However, the Doppler averaging (over 5 s) nearly matched its spin, thus reducing any periodic signature in the residuals. In the case of the Lunar Prospector tracking data, estimating a constant empirical along-track acceleration per arc was found to be beneficial to reduce the Doppler RMS of fit and to improve the quality of the gravity field solutions. This was especially true in the first 2 months of the nominal mission, when outgassing occurred (noted by *Konopliv et al.* [2001]); we obtained values consistent from arc to arc, which peaked at $\sim 2.5 \times 10^{-9}$ m/s$^2$, and the overlap errors between successive arcs were reduced by about one order of magnitude. The acceleration magnitudes decreased afterward, the mean dropping to nearly zero, but they continued to benefit the overlaps (although not as significantly, i.e., by less than a factor of 2).

## 2.2. Data Processing

[12] We use the radio tracking data from the following historical NASA lunar missions: Lunar Orbiters 1–5 (1966–1968), the subsatellites deployed by Apollo 15 and 16 (1971–1972), Clementine (1994) and Lunar Prospector (1998–1999). *Konopliv et al.* [2001] provided a detailed overview of the different types of data, tracking stations, and mission characteristics. Table 1 shows some general information in addition to time span: number of arcs we created, total number of data points, and approximate periapsis and apoapsis. In the case of Lunar Prospector, we followed *Konopliv et al.* [2001] and *Rowlands et al.* [2009], using an average arc length of 2 days. Those missions have a variety of semimajor axes, eccentricities, and inclination. The low-altitude ground track coverage and gravity field sensitivity of these different orbits are complementary, and enhance the separability of the gravity field coefficients in the least squares solutions.

[13] The primary radiometric data are Doppler observations of the transponder frequency from the orbiting spacecraft, sent from Earth and received at the same or a different Earth-based tracking station. Although range data are available, they are generally limited in quantity and accuracy. For Lunar Prospector, nearly 10% of the S-band data are range; however, their impact on the orbit solutions is slight. All the tracking data from the historical lunar orbits are S-band. We assigned an a priori data weight of 1 cm/s to the Doppler data of the Lunar Orbiters and the Apollo subsatellites, and of 1 mm/s to the Lunar Prospector data. The latter number is higher than that used by *Konopliv et al.* [2001], because we chose to put more emphasis on the representative arc RMS values than on the individual measurement noise. By doing this for both Doppler and range (5 m), we could select relative weights that tended to be consistent with what each data type actually brings to the adjusted orbits in terms of constraints.

## 2.3. Gravity Field Inversion

### 2.3.1. Preparation

[14] We created normal equations to degree and order 150 (150 × 150) in spherical harmonics for all satellites except Clementine, for which normal equations were created only to 75 × 75. The homogeneous normal equation size for the different lunar satellites helped ensure that the power spectrum of the solution would not manifest distortions at intermediate degrees as the result of truncation of signal. Clementine, with a periapsis near 400 km, has sensitivity to at most degree 30–35, so creating the normal equations to 75 is adequate and avoids these issues.

[15] We note that the expansion to $l = 150$ is not sufficient to exhaust the gravitational signal in some arcs, such as those of the Apollo subsatellites and the Lunar Prospector extended mission data. However, the creation of normal equations to $l = 200$ (for example) would be not only sig-

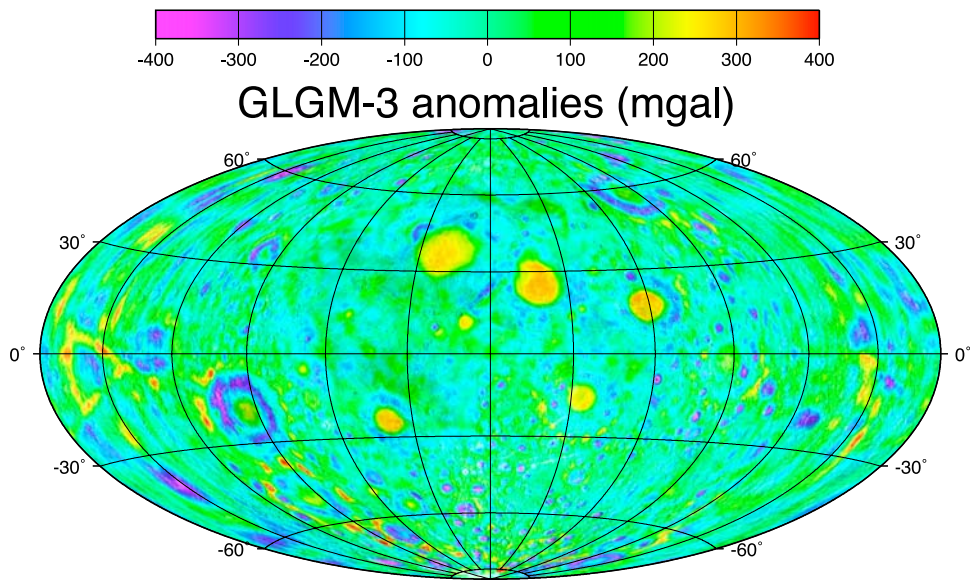


**Figure 1.** Hammer projection (centered at 0°E, 0°N) of the GLGM-3 gravity anomalies in milligals (1 mGal = $10^{-5}$ m/s$^2$). In Figures 1–11 the fields were truncated at degree l = 140 to remove aliasing.

nificantly more expensive computationally but also not necessarily the best way to extract the shorter-wavelength gravitational anomalies, given the total lack of information over the farside. A hybrid approach, using line-of-sight residuals of the Doppler data to bring regional improvements to a classically obtained spherical harmonics gravity field (such as described here), is more efficient [see *Han*, 2008].

[16] The normal equations associated with each spacecraft were combined into a single matrix by using the SOLVE program [*McCarthy*, 2008], part of the GEODYN II package. For Lunar Prospector, we aggregated the arcs for the nominal mission (mean altitude 100 km) and the extended mission (mean altitude 40 km) separately. The final effective data weights for each satellite are applied in SOLVE by scaling each aggregated matrix in the final least squares solution.

[17] Because all those normal equations are rank-deficient (obviously because of the farside data gap), gravity inversion cannot be performed without additional constraint (regularization). Failure to apply a regularization will cause the power spectrum of the gravity solution to deviate from a reasonable power law, and the coefficients at the higher degrees will have unnaturally high power. A power law constraint, or Kaula rule [*Kaula*, 1966], is commonly used to limit the power of the high-degree coefficients when the signal is not strong enough to lead to robust estimation. For each degree, the $C_{lm}$ and $S_{lm}$ coefficients are given a variance such that the total degree RMS is nearly $\sigma_l = K/l^n$. In the case of the Moon, because of the large farside data gap, it is preferable to apply a Kaula rule beyond degree $l \sim 10$. We use $K = 2.5 \times 10^{-4}$ and $n = 2$ on the basis of the power law of the LP165P solution of *Konopliv et al.* [2001]. In section 3.5 we discuss the impact of other power law constraints on the solution.

### 2.3.2. Gravity Field Solution

[18] Formal calibration of the gravity field proved difficult. Methods of optimal data weighting, such as that of *Lerch* [1991], use a master and a subset solution to assess whether the aggregate changes in the spherical harmonic coefficients are commensurate with the aggregate change in the coefficient standard deviations. This approach was applied in the development of the Earth satellite-only gravity solutions [e.g., *Lerch et al.*, 1994; *Lemoine et al.*, 1998]. However, the technique relies on the near-linearity of the solution, which is a problem for the Moon because the farside anomalies are largely unknown and the a priori solution is not necessarily expected to be close to truth. The procedure we followed did not lead to a satisfying solution, so instead we relied on orbital and geophysical performance as well as spatial resolution of the farside field to select a set of weights for the satellites making up the solution.

[19] *Lemoine et al.* [1997] used this calibration method, but at the time, Lunar Prospector data were not available, and the various tracking data sets all contributed relatively evenly to the solution. Owing to its global, low-altitude coverage, long mission duration, and high-quality tracking, Lunar Prospector completely dominates the gravity field solutions, which is very evident merely from the number of observations listed in Table 1. When a single data set exerts such dominance, we have found it difficult to apply the Lerch method of calibrations. We note that similar behavior was observed during the development of EGM96 [*Lemoine et al.*, 1998]. The satellite-only geopotential solution, EGM96S, included GPS data from a number of GPS satellites. After many tests, we found that the calibrations found with the Lerch method did not necessarily behave in a linear case.

[20] For each spacecraft data set, we chose the weights on the basis of the average observation RMS of fit of the arcs, instead of the noise level of the individual measurements. We then deweighted the data with respect to these average RMS of fit to prevent adverse effects on the solution arising from systematic errors (owing to force mismodeling) for a particular satellite. Some of the early lunar missions (Lunar Orbiter 1–3, Apollo subsatellites) are important to help

**Table 2.** Characteristics of the Data Sets Used for the Combined Normal Equations

| Spacecraft | Average Arc RMS of Fit (cm/s) | Final Effective Data Weight for GLGM-3 (cm/s) |
|---|---|---|
| Lunar Orbiter 1 | 0.24 | 3.16 |
| Lunar Orbiter 2 | 0.11 | 3.16 |
| Lunar Orbiter 3 | 0.07 | 3.16 |
| Lunar Orbiter 4 | 0.05 | 0.55 |
| Lunar Orbiter 5 | 0.21 | 0.49 |
| Apollo 15 subsatellite | 0.12 | 0.95 |
| Apollo 16 subsatellite | 0.15 | 0.32 |
| Clementine | 0.31 | 1.34 |
| Lunar Prospector (nominal) | 0.02 | 1.41 |
| Lunar Prospector (extended) | 0.25 | 3.78 |

resolve some of the large farside gravity anomalies (e.g., Korolev and Hertzprung) because their low inclination complements the meridionally integrated perturbations of the polar Lunar Prospector orbits (see also section 3.2). However, those spacecraft have lower quality data, and some orbits experience very large farside perturbations, such that excessive weighting leads to artifacts on the nearside. Also as discussed by *Konopliv et al.* [2001] and *Lemoine et al.* [1997], the Lunar Orbiter data are affected by uncoupled thruster jet firings to control the spacecraft attitude. These attitude maneuvers are explicitly modeled and parameters in the orbit solution are adjusted to accommodate them, but only when we have information that such attitude events might have occurred.

[21] Our preferred solution, the Goddard Lunar Gravity Model 3 (GLGM-3), is shown in Figure 1, and the data weights are given in Table 2. Some Lunar Orbiter data sets (1–3) were downweighted owing to their affecting the nearside negatively. To put an emphasis on the nearside short-wavelength features for the LRO mission, we slightly overweighted the Lunar Prospector extended mission in comparison with its ratio of observation fit over data noise. As we will show in section 3, GLGM-3 performs well with respect to a number of evaluation criteria. Even though it is not overwhelmingly better than other solutions from the same "family," which were obtained with alternative constraint and regularization methods (presented in section 3.5), GLGM-3 is the solution that can be best compared with previous work, because it relies on a standard inversion. This low sensitivity of the solution quality to the data constraint is a further sign of the robustness and stability of the inversion. The solution was not iterated; that is, we did not reconverge the data arcs, recreate normal equations, and perform the inversion again. Such procedures may be the focus of future work (section 4).

## 3. Discussion

### 3.1. Comparison With LP150Q

[22] Figure 2a presents various RMS degree spectra of gravity fields and of the potential from uncompensated topography (assuming a crustal density of 2900 kg m$^{-3}$ and an average density of 3340 kg m$^{-3}$). At lower degrees ($l \sim 20$), the power in GLGM-3 is well above that of the JPL solutions, likely reflecting the different strategies of data weighting and regularization that affect the farside. GLGM-3 and LP150Q agree well in power at high degrees, and both start to develop excess power owing to aliasing at $l \sim 140$. Their power spectra lie close to the uncompensated potential of ULCN 2005 [*Archinal et al.*, 2006], which is interesting because at high degrees the topography is expected to be mostly uncompensated. However, the more recent and accurate SELENE LALT topography shows much higher power. This difference is in part due to the farside/nearside dichotomy, the more sparsely sampled farside being the main driver of the global power spectrum. When localizing those spectra hemispherically (the nearside defined as an 80° cap centered on 0°N,0°E, and the farside defined as its complementary region), the deficit in nearside gravity field power begins only near $l \sim 100$ (Figure 2b), compared with near $l \sim 20$ on the farside (Figure 2c).

[23] Those hemispherical uncertainties were obtained after localizing the full covariance matrix (including off-diagonal terms), as described by *Han et al.* [2009]. The shape of the localized sigma spectrum over the nearside (Figure 2b) is similar to what has been observed for Mars [*Lemoine et al.*, 2001] and for the Moon with the SELENE four-way tracking data. Figure 2b also shows the nearside differences with LP150Q (Gravity Science Team, 2000, using the same data sets). For $l > 30$, they are small, comparable with the predicted uncertainties (see section 3.2). For lower degrees, the differences are much larger than predicted by this localization method. Discrepancies with the observed field-to-field differences could result from optimistic formal errors, because nonlinearities induced by the farside gap are not properly captured in the covariance matrix.

[24] Spatially, those differences are concentrated near the limbs and the poles (Figure 3). This in part reflects our different approach to the data weighting of the Lunar Prospector data set. Because most of the tracking data of the Lunar Prospector mission was acquired from an omnidirectional antenna, signal multipath effects near the pole during the extended mission at lower altitude lead to higher noise when recorded by ground stations. Instead of increasing the data noise within each arc, we put less weight on the normal equations created with the extended mission arcs. *Konopliv et al.* [2001] applied a latitudinal deweighting function, which had a maximum value of 50 for points within 1° of the poles. The idea was to compensate for the convergence of the ground tracks near the poles and the potential oversampling overinformation. We did not apply this deweighting function to the Doppler observations, a strategy that appears to be partly responsible for improvements near the poles (section 3.4).

[25] However, the large basins in the low latitudes of the farside are better resolved with LP150Q, although both fields considerably lack resolution in comparison with the solution obtained with the four-way SELENE tracking data [*Namiki et al.*, 2009]. Whereas the Lunar Prospector data are the major constraint for the nearside field to the highest degrees, its polar inclination prevents the localization in latitude of the farside anomalies. Only when combined with data of the low-inclination satellites (Lunar Orbiters, Apollo subsatellites) can the observed hemispherically integrated orbit perturbations spatially constrain the location of the gravitational anomalies. The large long-wavelength features are due to higher power at low degrees ($l \sim 10$; see Figure 2c) and are not necessarily significant because they occur mostly

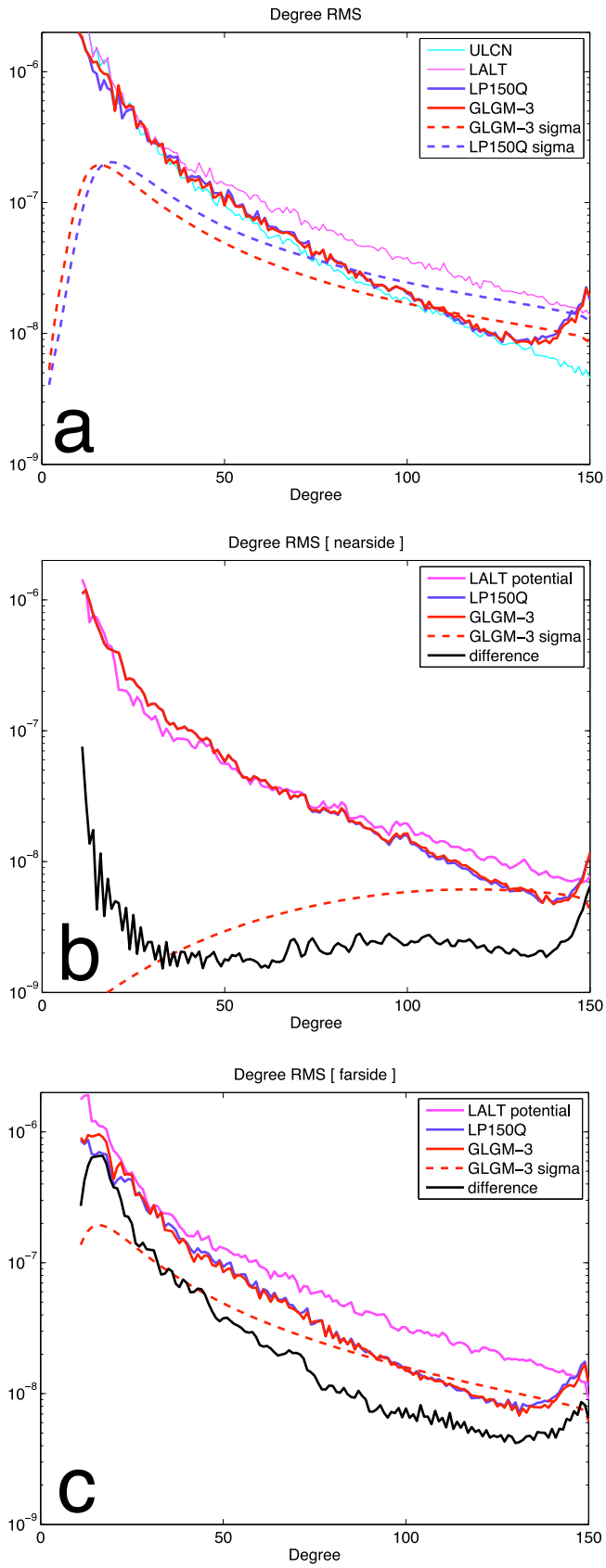


**Figure 2.** (a) Degree RMS spectrum of potential from uncompensated topography (ULCN-2005 and SELENE/LALT), gravity fields (LP150Q and GLGM-3), and formal uncertainties of GLGM-3. (b) Nearside-localized degree RMS spectrum of the potential from uncompensated SELENE/LALT topography, of the LP150Q and GLGM-3 gravity fields and their difference, and of the formal uncertainties of GLGM-3. (c) Same as Figure 2b, localized on the farside.

at nonequatorial latitudes with few favorable spacecraft inclinations. The error spectra shown in Figures 2b and 2c confirm a comment in the work of *Konopliv et al.* [2001] stating that most of the aliasing observed and the error spectrum were due to the farside data gap.

### 3.2. Spatial Error Estimation

[26] We used the (full) error covariance matrix to quantify the formal uncertainty of the gravity field estimates in the spatial domain by performing an error propagation up to degree and order 100. The estimated errors in surface gravity anomalies (Figure 4) closely follow the tracking data coverage, with the lowest errors on the nearside, moderately higher errors near the limbs (where coverage was reduced owing to lunar librations or owing to direct radio link only at high altitudes). Over the farside, as observed previously, the equatorial region shows lower errors than the high latitudes, because of the many early low-inclination orbiters, which enable the spatial determination of large anomalies. These formal uncertainty estimates (9 ± 3 mGal for the nearside; 38 ± 22 mGal for the farside) are a bit lower but consistent with those quoted by *Konopliv et al.* [2001] for LP165P (which were calculated up to degree and order 110).

[27] It is interesting to see how important each spacecraft is to the combined solution. The different panels in Figure 5 show the reduction in formal error between a solution without and with a given spacecraft. The extended mission of Lunar Prospector is the single most important data set, but the nominal mission is important for the limb regions, where the spacecraft could be tracked while orbiting at 100 km, but not near 50 km. The other satellites contribute little to the nearside but are important for improving the farside. An exception is Apollo 16, whose very low altitude and low-inclination orbits contribute to low formal errors in the equatorial region even when Lunar Prospector extended mission data are used (Figure 5).

### 3.3. Orbit Performance

#### 3.3.1. Residuals

[28] A common measure of the quality of a gravity field solution is the improvement of the observation fit. Given that our a priori field is to degree and order 100 (LP100K), we can expect improvements for altitudes less than 110 km. The results for Lunar Prospector (the spacecraft with the most radio tracking and the most consistent arcs for evaluation) are plotted on Figure 6. To first order, the results are similar to those obtained with LP150Q, that is, modest in the nominal phase and significant in the extended phase. Actually, Lunar Prospector provides a slight yet consistent improvement over LP150Q both in the nominal phase (~90% of the arcs) and in the low-altitude extended phase

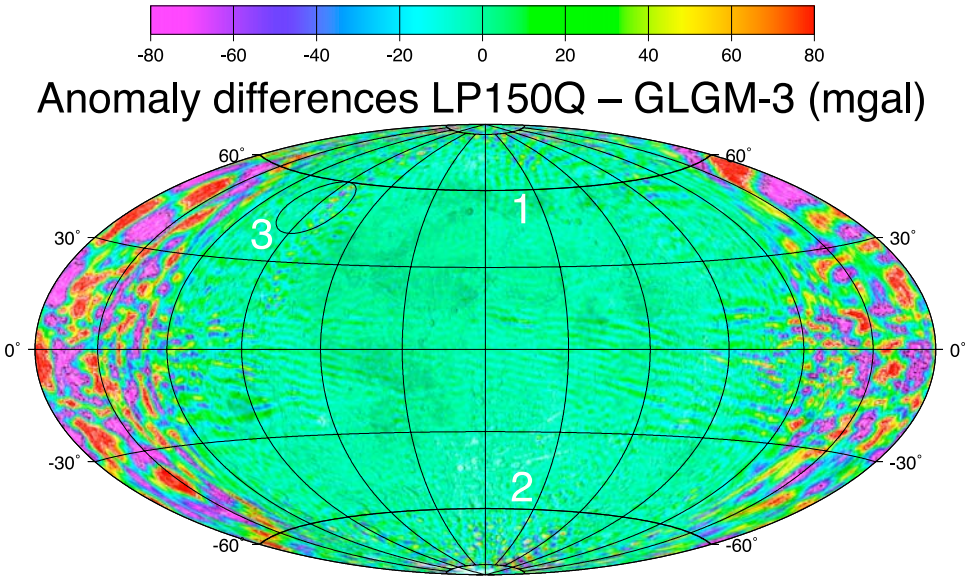


**Figure 3.** Hammer projection (centered at 0°E, 0°N) of the differences between LP150Q and GLGM-3 in milligals. Note the regions 1–3, referred to in sections 3.4 and 3.5 and in Figures 8–9.

(~70% of the arcs). However, we note that the LP150Q solution was developed with different models, a different inversion scheme, and a different orbit determination program. In particular, the LP100K and LP150Q fields were obtained by using the DE403 ephemeris [*Standish et al.*, 1995]. As noted in the work of *Williams et al.* [2008], the small changes in principal axes contribute only to position differences at the meter level. Tests conducted on Lunar Prospector arcs indicate that using LP100K and LP150Q with the newer DE421 ephemeris marginally affects the residual values. The Doppler RMS increases by less than 0.5% on average with LP100K, and by about 1% with LP150Q, while the range values show smaller, often beneficial changes. The extended mission appears to be less sensitive, probably because of the significantly higher residuals than during the nominal phase. Our solution performs better with the models from which it was obtained, but one should be careful not to overinterpret these improvements.

[29] Another interesting way to evaluate the observation fit is, instead of looking at a single value for each arc like the residual RMS, plotting them spatially. Here, we use the differences between sequential Doppler residuals to create line-of-sight accelerations (in milligals). Figure 7 shows the difference between these accelerations after convergence with LP150Q and with GLGM-3, over restricted altitude ranges (100–110 km for Figure 7a; 40–50 km for Figure 7b). The color tone indicates which gravity field has the lowest residual value (red for LP150Q, green for GLGM-3).

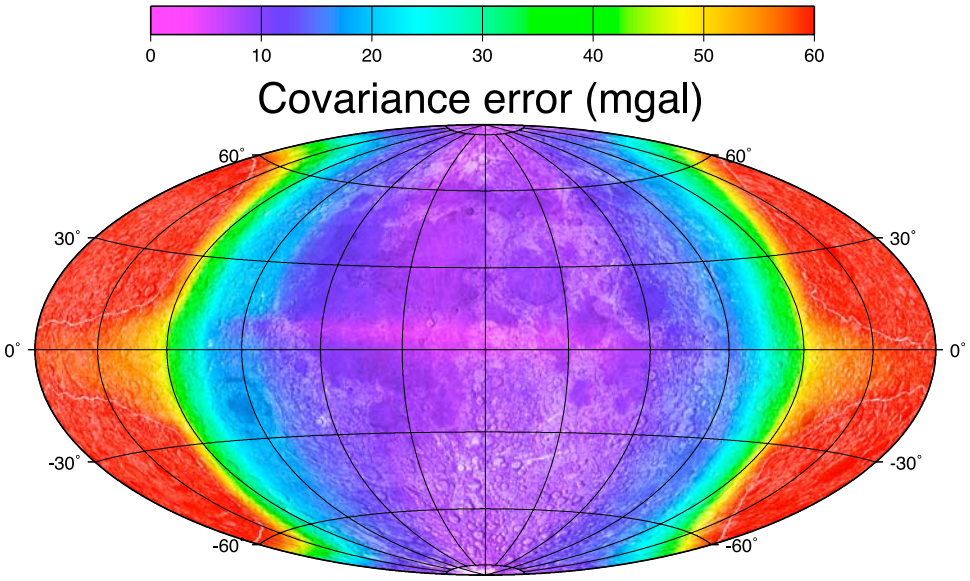


**Figure 4.** Hammer projection (centered at 0°E, 0°N) of the gravity a nomaly uncertainties estimated by propagating the covariance matrix (up to degree and order 100).

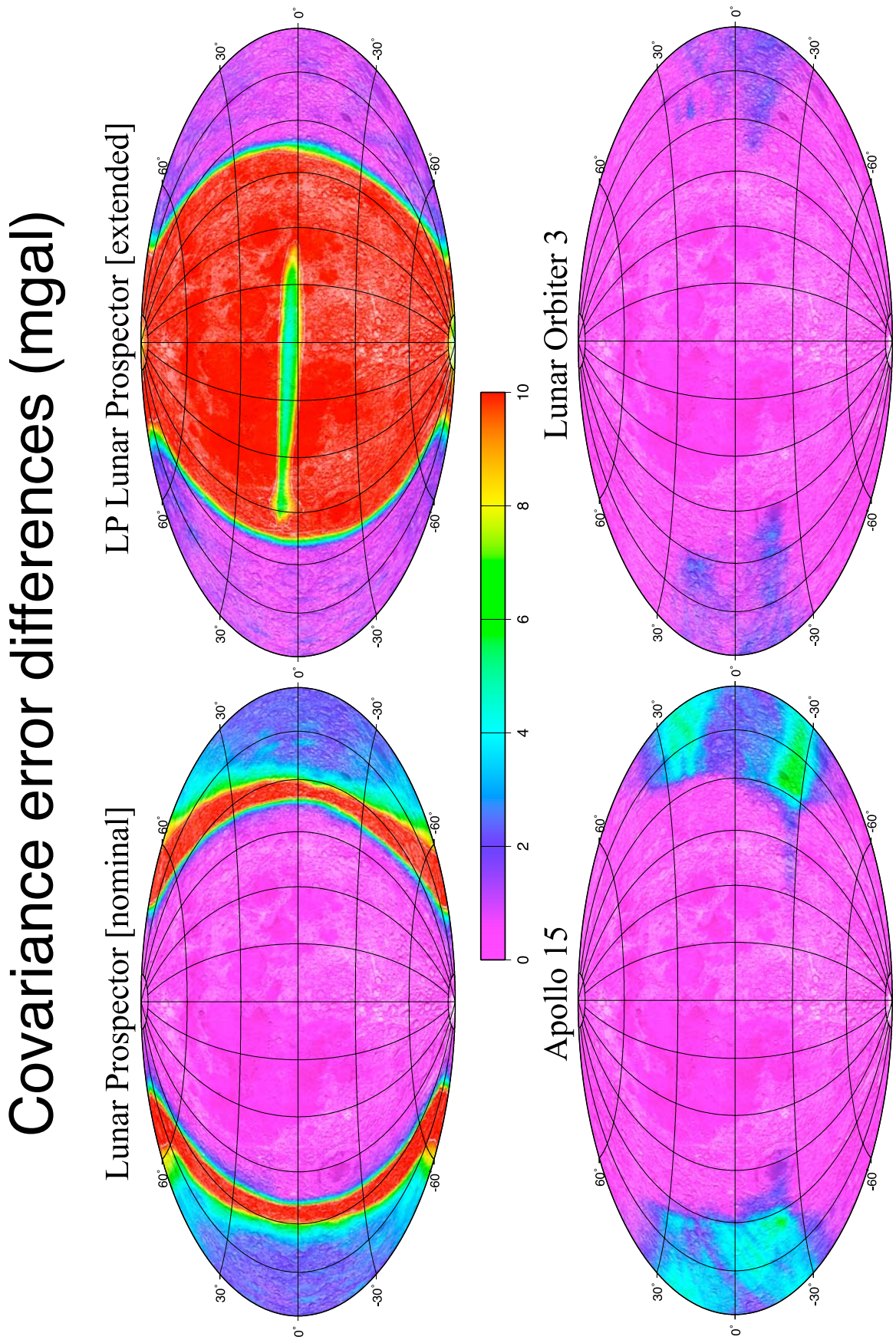


**Figure 5.** Hammer projection (centered at 0°E, 0°N) of the reductions in gravity anomaly uncertainties attributable to selected individual data sets. The covariance matrices were propagated up to degree and order 100.

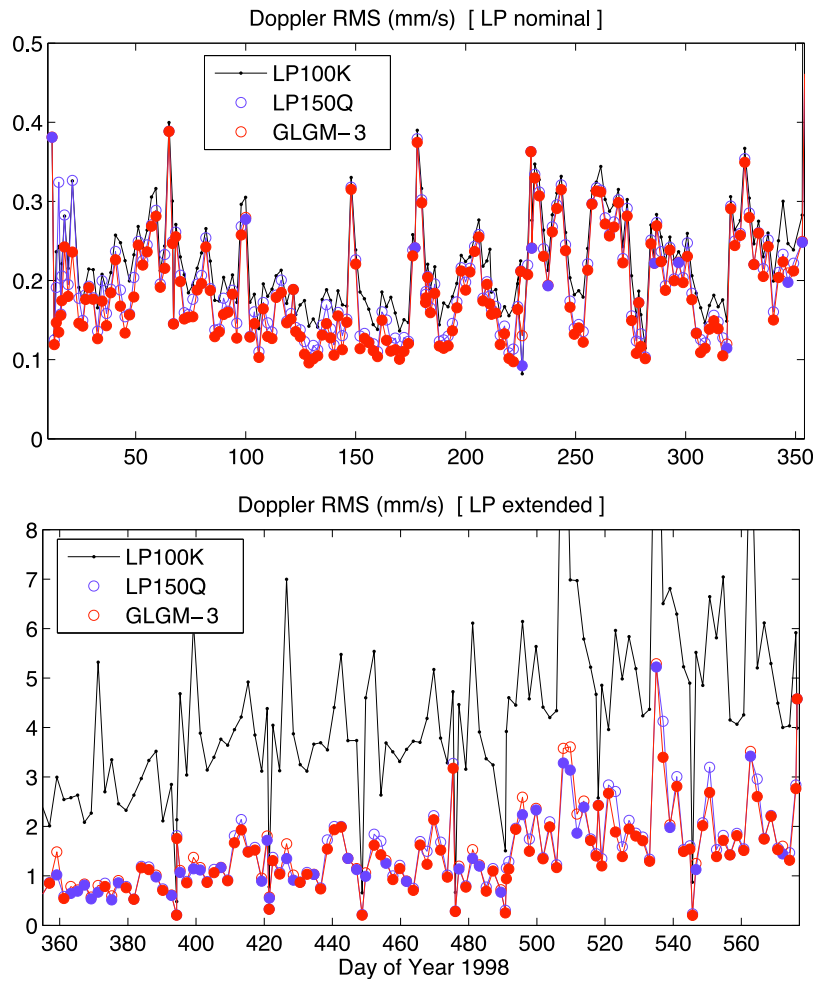


**Figure 6.** RMS of the Doppler (range-rate) observations (in millimeters per second) of each Lunar Prospector arc, during its (top) nominal and (bottom) extended phases. The a priori field (LP100K) is shown in black, LP150Q in blue, and GLGM-3 in red. Circles are filled when the field performs better than the other.

GLGM-3 performs better in the nominal phase, but by only a small margin (~1% of the ±0.2 mGal scale displayed). The sectorial pattern results from the polar orbit of LP and the arc length (2 days). A better fit by either gravity model usually results in the majority of the residuals of an arc being lower. The radial component of the line-of-sight accelerations is also expected to be larger near the equator, resulting in paler colors near the poles.

#### 3.3.2. Prediction Overlaps

[30] We used the Lunar Prospector data set to evaluate the changes in orbit prediction from the a priori model. The 2 day arcs were forward-propagated for 6 h, without any tracking data. Differences in the trajectories of adjacent arcs that overlapped during this 6 h period were evaluated.

[31] The changes with respect to LP100K are modest in the nominal phase of the Lunar Prospector mission. The average overlaps of ~0.8, ~3, and ~11 m in the s are reduced by ~0.2, ~0.9, and ~1.4 m, respectively. In the low-altitude extended phase, where the lower-degree a priori model is expected to have more difficulties in orbit propagation than will a higher-altitude model, the average radial, transverse, and normal direction overlaps (~5.3, ~31, and ~83 m) are significantly improved, decreasing to ~2.9, ~16, and ~54 m, respectively. The LP150Q model performs better in the extended phase, on average (~2.4, ~13, and ~42 m, respectively). However, we note that LP150Q does not consistently show smaller orbit differences; in one third of the extended mission arcs, GLGM-3 performs better.

### 3.4. Geophysical Performance

[32] The geophysical performance of a gravity field is an important measure of its quality, because it uses an independent data set, topography. At the resolution required here, the uncertainties in the geolocated topographic points, caused in part by gravitational perturbations, are insignificant. We use the recent SELENE LALT topography [*Araki et al.*, 2009], which has global coverage and consistent precision (~10 m vertical), unlike the earlier ULCN 2005 [*Archinal et al.*, 2006], which merged control points derived from stereophotography and Clementine laser altimetry data [*Smith et al.*, 1997]. As shown in the work of *Han et al.* [2009], the LALT topography yields more robust results.

[33] Except at low degrees, where large-scale geophysical processes operate, gravity and topography are expected to

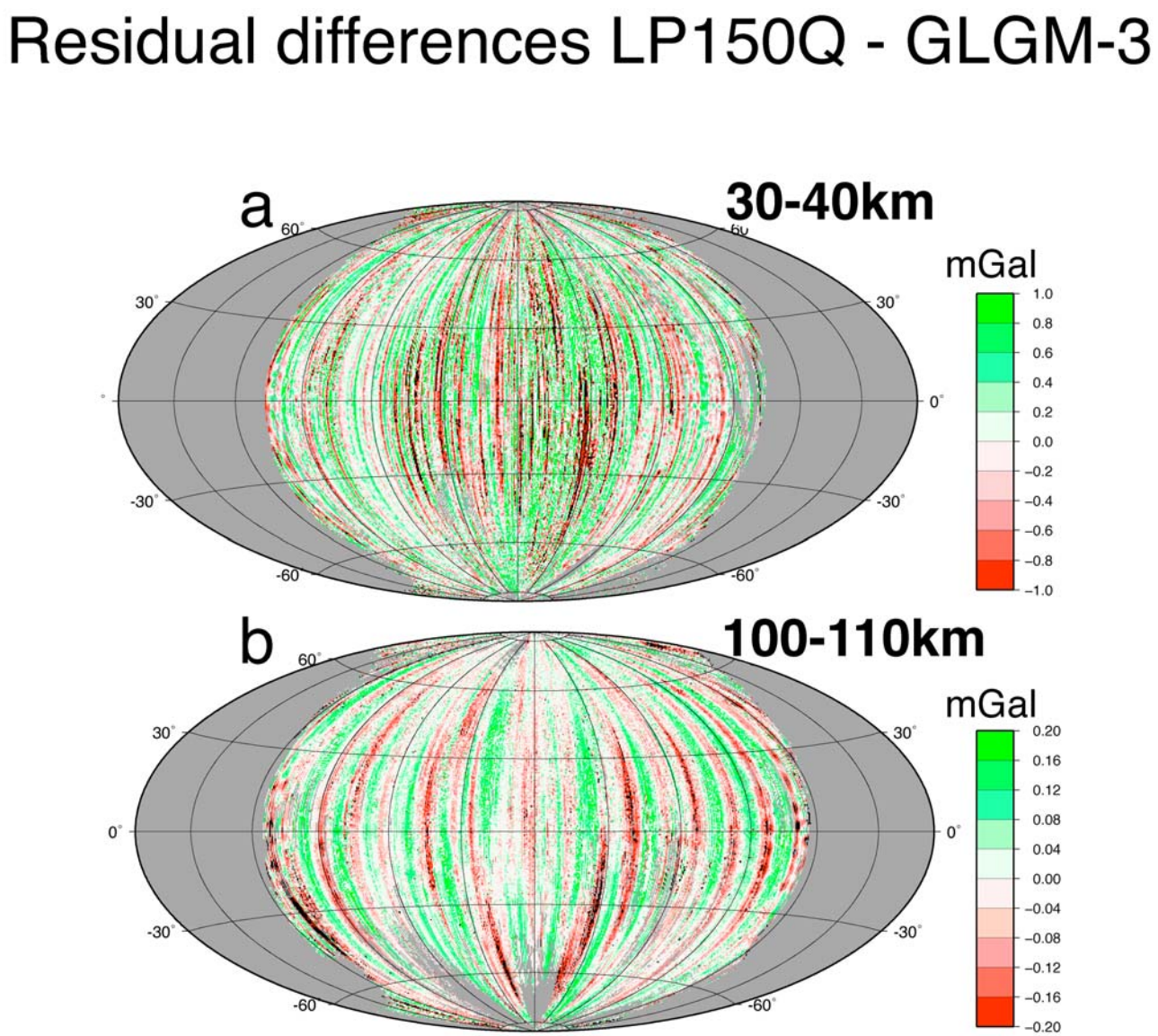


**Figure 7.** Hammer projections (centered at 0°E, 0°N) of the differences in median residual line-of-sight Lunar Prospector accelerations (i.e., differences in Doppler residuals) between the LP150Q and GLGM-3 gravity fields. Green indicates that LP150Q has larger unmodeled accelerations. Only data within a given altitude range are used: (a) 30–40 km, corresponding to the extended mission, and (b) 100–110 km, the nominal mission. The scale bar is ±1 mGal in Figure 7a and ±0.2 mGal in Figure 7b.

be related. In the case of the Moon, large-scale geophysical processes (e.g., mascons, large impact basins, potential mantle convection) dominate the $l = 5$–20 range [*Muller and Sjogren*, 1968], but at higher degrees the gravity is expected to generally result from the amount of crustal material and hence the topography. In addition to assessing the topographic spectrum, correlation, and admittance globally, we evaluate them hemispherically (nearside and farside) and regionally (see the three regions defined in Figure 3).

#### 3.4.1. Topography Correlation

[34] Because short-wavelength loads on the elastic lithosphere will not produce significant bending and compensation, the observed gravitational signal will be closely related to the topography, except in zones with local tectonics. Thus, a large correlation coefficient at high degrees is usually interpreted as a sign of quality of the gravity field, accurately reproducing the signal of mostly uncompensated topography. Previously, because of the lack of reliable global topography at high degrees, the correlation dropped off early and could not be used effectively. However, the new LALT topography shows improved correlation for $l >$ 100 with the degree-150 fields compared with correlations obtained with our a priori field, LP100K. When the fields are localized hemispherically, only the nearside shows real improvement (Figure 8a). The very poor and partly negative correlation at low degrees over the nearside has been observed previously and interpreted as overcompensation of the mascons [*Neumann et al.*, 1996]. In the global and nearside correlation, we observe slight improvements over the LP150Q solution at very high degrees, which are also

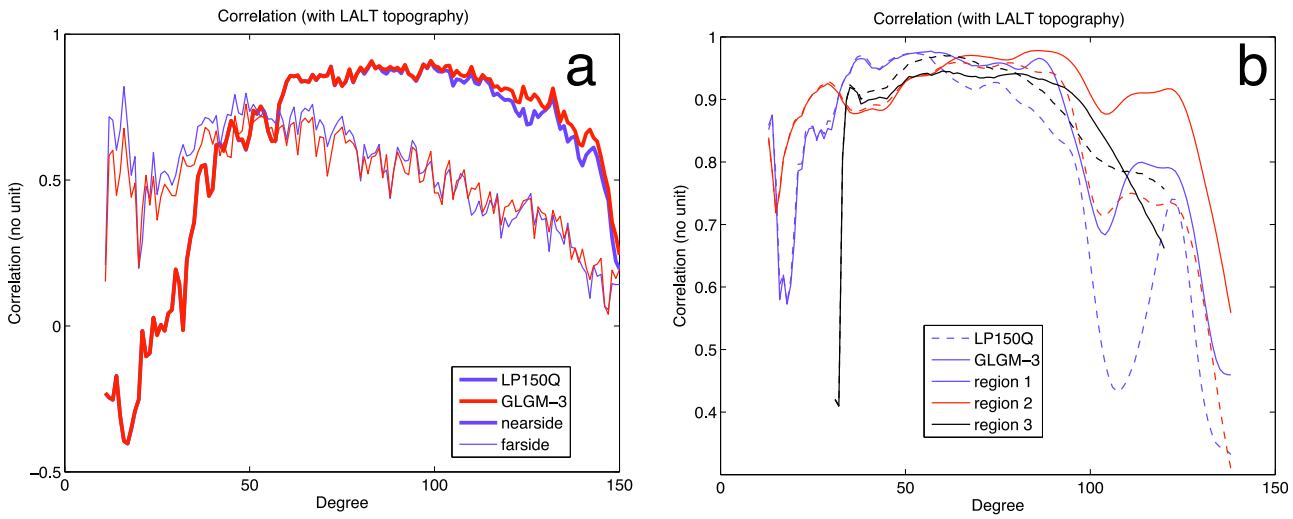


**Figure 8.** Correlation of the LP150Q and GLGM-3 gravity fields with the SELENE/LALT topography, localized in various regions: (a) nearside and farside (thin and thick lines, respectively) for GLGM-3 (red) and LP150Q (blue); (b) smaller spherical cap regions (various colors), indicated in Figure 3, for GLGM-3 (solid line) and LP150Q (dashed line).

seen at more regional scales (Figure 8b). The different weighting scheme of the Lunar Prospector range-rate data might explain those differences, as could potentially a smaller weight given to the Apollo subsatellites (which can help improve the farside gravity but can create stripe artifacts on the nearside; see Figure 3).

#### 3.4.2. Admittance

[35] The admittance is the transfer function between gravity to topography. For the same reasons as above, the uncompensation of short-wavelength topography should lead to admittance values stabilizing at high degrees (at a level related to the density of the crust). Figure 9 shows the admittance calculated for the LP100K, LP150Q and GLGM-3 fields in various regions. The same observations can be made as for the correlation (GLGM-3 generally performing better than LP150Q at high degrees on the nearside, and worse at low degrees on the farside), but all fields show a significant decrease compared with the expected flattening at high degrees (starting at $l - 80$ on the nearside and $l - 40$ on the farside; see Figure 9a). The overcompensation of the nearside mascons is clearly visible at low degrees on Figure 9b (region 3, defined in Figure 3).

### 3.5. Other Solutions

[36] We describe various gravity field solutions obtained with the same data set, but using other inversion strategies. For the most part, these solutions perform similarly to GLGM-3 in terms of data fit (that is, over the nearside, where data are available) and overlap analysis. Nevertheless, these are important experiments, and pursuing them with new data can be worthwhile. For our detailed comparison with LP150Q above, we think GLGM-3 was the most

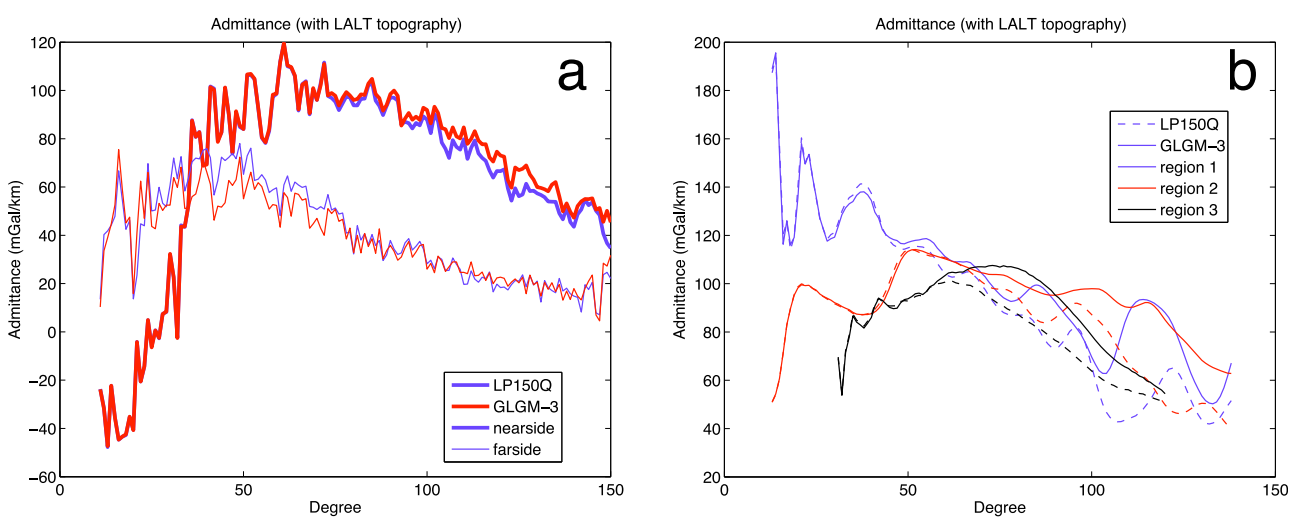


**Figure 9.** Same as Figure 8, but admittance (in milligals per kilometer) is plotted.

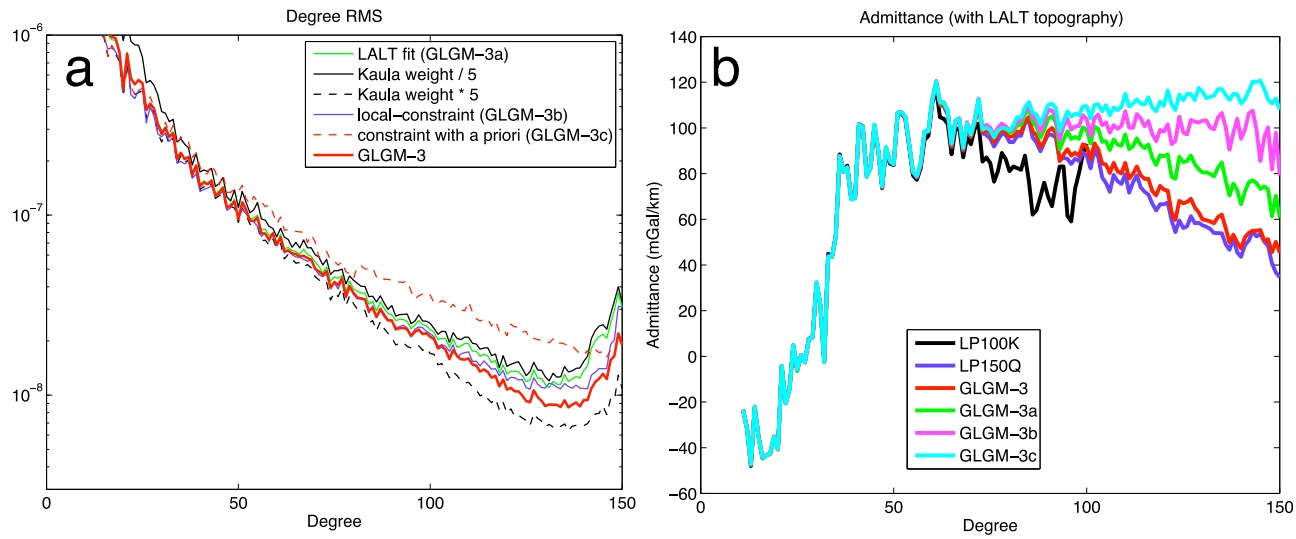


**Figure 10.** (a) Degree RMS spectra and (b) admittance of the various gravity field solutions obtained with alternate constraints or techniques.

appropriate field, because of its similar inversion method. But this family of solutions can be used to assess the variability of outcomes owing to technical inversion approach. The comparison of results from such related models could be beneficial, for instance, in mission planning or orbital prediction error studies.

#### 3.5.1. Varying Kaula (GLGM-3a)

[37] As explained in section 2.3.1, the application of a power law constraint (Kaula rule) is necessary to obtain a reasonable lunar gravity solution. We assess the impact of the power law on the solutions by varying the weight of the power law. The power law is applied as an additional (diagonal) matrix in the least squares solution. By changing the scale factor, we effectively assess the impact of weaker or stronger power law constraints.

[38] We first changed the weighting given to the power law. A fivefold reduction leads to larger power at high degrees on the nearside, improving correlation and admittance, but the solution is very degraded on the farside at low degrees. However, an increase reduces the short-wavelength power on the nearside, which is already depleted in comparison with uncompensated SELENE/LALT potential (Figure 2).

[39] In addition, we fitted a power law to this topography potential to replace the (common) $l^{-2}$ constraint (the fitted values are $K = 2.1 \times 10^{-4}$ and $n = 1.88$), and obtained a new gravity field, GLGM-3a (Figure 10). On the nearside, we see a similar power spectrum. Correlation begin to differ at around $l = 100$ near the poles and $l = 60$ in region 3 (from Figure 3), but only marginally. Admittance is improved in the North Pole region ($l > 110$), but only slightly near the South Pole ($l > 120$). In region 3, differences arise at longer wavelength ($l \sim 60$); the change in admittance is highest near $l = 80$ and becomes insignificant for $l > 110$. More power is present over the farside than in the GLGM-3 solution, because of the looser Kaula rule.

#### 3.5.2. Localized Constraint (GLGM-3b)

[40] As discussed previously, the lack of direct tracking data over the Moon's farside presented an important problem for gravity solutions. Newly obtained indirect (four-way) radio tracking data of the SELENE mission greatly improved resolution of the farside gravity anomaly and will be quite valuable once they become available. Otherwise, the use of a power law constraint during inversion to limit the power of the numerous high-degree expansion coefficients is necessary.

[41] However, *Han et al.* [2009] showed that the nearside field is seriously affected and biased when this constraint is applied globally. They performed the inversion with an alternate set of localized spherical harmonics basis functions, which allowed the power law constraint to be applied only on the coefficients with power concentrated on the farside. We applied this technique here with the same data sets and weights as GLGM-3, and obtained a local-constraint gravity field, GLGM-3b. It differs from the gravity field published by *Han et al.* [2009], because of additional data sets (Lunar Orbiter 1–3) and a slightly different weighting scheme. Although the farside field is visually nearly identical to previous (globally constrained) solutions, the nearside field has more power at high degrees ($l > 100$; see Figure 10). Correlation and admittance showed significant improvements. In particular, over the nearside and over smaller regions (Figure 3), the admittance is stable up to very high degrees ($l \sim 140$, comparable to the maximum expected resolution before aliasing). The correlation is most significantly improved near the North Pole, gaining nearly 0.1 in the $l = 90$–$110$ band.

[42] NASA's GRAIL mission, to be launched in 2011, will bypass the Earth tracking-geometry issues by having two identical spacecraft track one another continuously and provide uniform high-precision coverage [*Zuber et al.*, 2008]. Until then, this constraint localization technique will be valuable when producing new gravity fields (e.g., with LRO low-altitude data).

#### 3.5.3. A Priori Bias Constraint (GLGM-3c)

[43] If we assume that short-wavelength topography is uncompensated (and that crustal density is uniform), we can predict its contribution to the gravitational potential at high degrees and use it to constrain the gravity field. However, because of all this imposed a priori information, the corre-

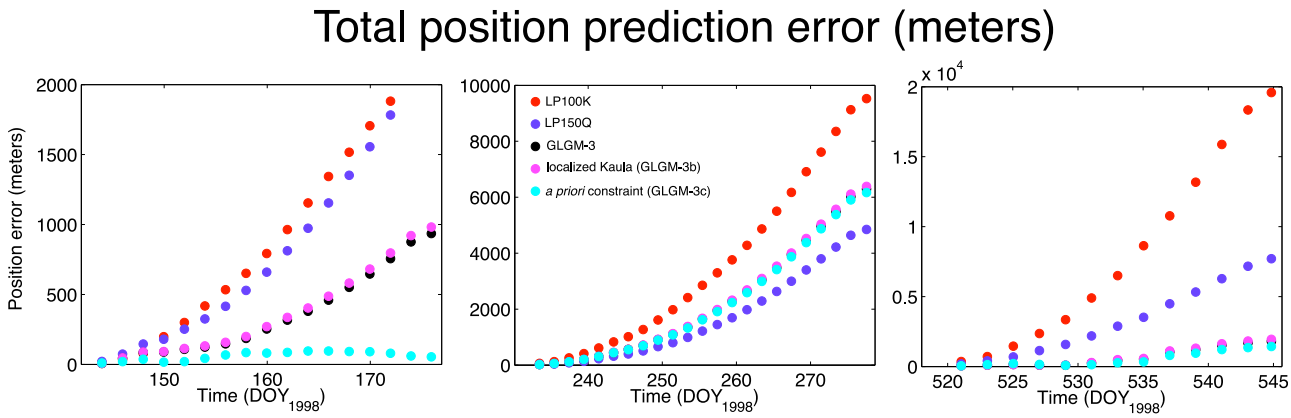


**Figure 11.** Error in prediction position when using various gravity fields. Shown are the three different periods of ~30 days. In the middle panel, prediction errors from GLGM-3 and GLGM-3b are nearly equal.

lation of the field with topography is expected and thus is not diagnostic of the contribution of the tracking data. The increased resolution, of the farside in particular, can be beneficial to orbital performance.

[44] The common Kaula rule used to regularize the least squares inversion is modified: instead of an expectation value for each coefficient of zero, expansion coefficients' a priori values are set to the SGM90d gravity field up to degree-80, and the potential from uncompensated SELENE/LALT topography is used at higher degrees. But the a priori constraint on the coefficient variances is identical to the global constraint used in GLGM-3. The spherical harmonics expansion coefficients of SGM90d were calculated from the gridded map published by *Namiki et al.* [2009].

[45] Over the farside, the resulting field (GLGM-3c) differs from the a priori constraint at intermediate wavelengths (where there are constraints from the data). On the nearside, the current field (GLGM-3c) is close, though not identical in some areas and at high degrees, to that obtained with GLGM-3. In particular, artifacts due to the low-inclination orbits of the Apollo and Lunar Orbiter spacecraft appear near the limbs (similar to those seen in Figure 3). As expected, over the nearside, correlation (not shown) and admittance (Figure 10) are improved. Regionally, the admittance is significantly better (flattening at high degrees, as expected from uncompensated topography) over both poles. The gravity field is also improved in region 3, but after leveling between $l \sim 80$ and $l \sim 100$, we note a decline due to loss of power for $l > 100$. The correlation is improved over region 3 at short wavelength ($l > 70$), with increases over already high levels in both the north and south polar regions for $l > 90$ (up to 0.2 near $l = 100$ and 0.07 near $l = 110$, respectively).

[46] Unfortunately, the field does not perform better than GLGM-3 in terms of Doppler RMS for arcs of the Lunar Prospector extended mission (the only data set that still has observation fit higher than the data noise level). Of course, only the nearside can be evaluated with this criterion because of the lack of data over the farside. An increase in the field resolution ($l_{max}$) and more farside data coverage are probably necessary.

[47] However, the orbit prediction capability is improved with this high-resolution topographic information. The trajectory of an initial 2 day arc, reconstructed with tracking data, was propagated for one additional month, with no data input. The predicted trajectory was then compared with a sequence of 2 day arcs spanning that entire month, each converged with radio tracking data. Figure 11 shows the total position errors obtained with various gravity fields, over three distinct periods. The a priori constraint consistently improves the predictions by GLGM-3, usually by a small amount but in one case (Figure 11, left) significantly. However, in cases when LP150Q has a better prediction capability than GLGM-3, the additional constraints from topography are not sufficient to reverse this pattern. Independent orbits and data from the LRO mission will enable us to better evaluate the prediction quality of those fields.

## 4. Conclusion and Future Work

[48] The main purpose of this work was to prepare for the LRO mission, and the quality of the normal equations produced appears to be satisfactory. The GLGM-3 gravity solution, based on the same data as the JPL LP150Q, shows good agreement with that field, which is widely used as reference in the lunar science community. Quantitatively, the levels of data fit are nearly identical. With our orbit determination setup, their orbital performance is similar. Also, while GLGM-3 lacks some resolution on the farside, it does offer improved correlation and admittance on the nearside and polar regions. Qualitatively, the anomalies (expanded to degree and order 140) over the nearside do not show artifacts or aberrations, their correspondence with geophysical features is good, down to very small scales.

[49] The addition of LRO radio tracking data when they become available will help improve the determination of the nearside gravity anomalies. Future work may include further use of the local-constraint technique mentioned above; for example, data sets important for farside resolution could be given a lower weight in the nearside region, where their use can produce artifacts. As evidenced by the lack of improvement in the arc RMS of Lunar Prospector with the various gravity fields, an inversion to higher degrees might be necessary to make further headway. Hybrid models, built globally by the inversion of a set of normal equations and regionally refined by line-of-sight techniques [e.g., *Han*, 2008], will be explored.

[50] We are also considering the use of GLGM-3 as the a priori gravity field to create a new set of normal equations for all the tracking data (an iteration of the solution). Provided the LRO LOLA altimetric crossover constraints are strong [*Mazarico et al.*, 2010], the constraints could be used as data, and give further constraints on the farside field, before the GRAIL mission provides high-resolution global coverage and to some extent "solves" the problem of selenodesy.

[51] **Acknowledgments.** E.M. was supported by an appointment to the NASA Postdoctoral Program at the NASA Goddard Space Flight Center, administered by Oak Ridge Associated Universities through a contract with NASA. S.C.H. was supported by NASA's programs in Lunar Advanced Science and Exploration Research and Mars Data Analysis. We acknowledge the Planetary Data System/Geosciences Node for providing the Lunar Prospector tracking data, and Alex Konopliv (JPL) for answering questions related to the interpretation of the Lunar Prospector orbit data files. David Rowlands (NASA Goddard Space Flight Center), Despina Pavlis, and John McCarthy (NASA Goddard Space Flight Center and SGT, Inc.) provided indispensable technical support with GEODYN and SOLVE. We acknowledge Jim Williams and colleagues at JPL for making available DE421. We thank the Lunar Reconnaissance Orbiter project for their support of this work.

## References

Araki, H., et al. (2009), Lunar global shape and polar topography derived from Kaguya-LALT laser altimetry, *Science*, *323*, 897–900, doi:10.1126/science.1164146.

Archinal, B. A., M. R. Rosiek, R. L. Kirk, and B. L. Redding (2006), The unified lunar control network 2005, *U.S. Geol. Surv. Open File Rep. 2006–1367*.

Chin, G., et al. (2007), Lunar Reconnaissance Orbiter Overview: The instrument suite and mission, *Space Sci. Rev.*, *129*, 391–419, doi:10.1007/s11214-007-9153-y.

Dick, W. R., and B. Richter (2008), IERS Annual Report 2006, 187 pp., Int. Earth Rotation and Ref. Syst. Serv., Frankfurt, Germany.

Floberghagen, R., P. Visser, and F. Weischede (1999), Lunar albedo force modeling and its effect on low lunar orbit and gravity field determination, *Adv. Space Res.*, *23*, 733–738, doi:10.1016/S0273-1177(99)00155-6.

Goossens, S., and K. Matsumoto (2008), Lunar degree 2 potential Love number determination from satellite tracking data, *Geophys. Res. Lett.*, *35*, L02204, doi:10.1029/2007GL031960.

Goossens, S., K. Matsumoto, N. Namiki, H. Hanada, T. Iwata, S. Tsuruta, N. Kawano, and S. Sasaki (2006), Global lunar gravity field determination using historical and recent tracking data in preparation for SELENE, *Eos Trans. AGU*, *87*(52), Fall Meet. Suppl., Abstract G52B-01.

Han, S.-C. (2008), Improved regional gravity fields on the Moon from Lunar Prospector tracking data by means of localized spherical harmonic functions, *J. Geophys. Res.*, *113*, E11012, doi:10.1029/2008JE003166.

Han, S.-C., E. Mazarico, and F. G. Lemoine (2009), Improved nearside gravity field of the Moon by localizing the power law constraint, *Geophys. Res. Lett.*, *36*, L11203, doi:10.1029/2009GL038556.

Kaula, W. M. (1966), *Theory of Satellite Geodesy*, 124 pp., Blaisdell Publ., London.

Knocke, P. C. (1989), Earth radiation pressure effects in satellites, Ph.D thesis, Univ. of Texas at Austin, Austin.

Knocke, P. C., J. C. Ries, and B. D. Tapley (1988), Earth radiation pressure effects on satellites, paper presented at the AIAA/AAS Astrodynamics Specialist Conference, Am. Inst. of Aeron. and Astronaut., Boston, Mass.

Konopliv, A. S., W. L. Sjogren R. N. Wimberly, R. A. Cook, and A. Vijayaraghavan (1993), A high-resolution lunar gravity model and predicted orbit behavior, paper presented at the AIAA/AAS Astrodynamics Specialist Conference, Am. Inst. of Aeron. Astron., Victoria, B. C.

Konopliv, A. S., S. W. Asmar, E. Carranza, W. L. Sjogren, and D. N. Yuan (2001), Recent gravity models as a result of the Lunar Prospector Mission, *Icarus*, *150*, 1–18, doi:10.1006/icar.2000.6573.

Lawson, D. L., and R. J. Hanson (1974), *Solving Least Squares Problems*, Prentice-Hall, Englewood Cliffs, N. J.

Lemoine, F. G., D. E. Smith, M. T. Zuber, G. A. Neumann, and D. D. Rowlands (1997), GLGM-2: A 70th degree and order lunar gravity model from Clementine and historical data, *J. Geophys. Res.*, *102*, 16,339–16,359, doi:10.1029/97JE01418.

Lemoine, F. G., et al. (1998), The development of the joint NASA GSFC and the National Imagery and Mapping Agency (NIMA) geopotential model EGM96, *Rep. NASA/TP-1998–206861*, NASA Goddard Space Flight Cent., Greenbelt, Md.

Lemoine, F. G., et al. (2001), An improved solution of the gravity field of Mars (GMM-2B) from Mars Global Surveyor, *J. Geophys. Res.*, *106*, 23,359–23,376, doi:10.1029/2000JE001426.

Lemoine, F. G., D. D. Rowlands, E. Mazarico, D. S. Chinn, J. McGarry, and M. H. Torrence (2008), Precision orbit determination for the Lunar Reconnaissance Orbiter (LRO), paper presented at 37th COSPAR Assembly, Montreal, Que.

Lerch, F. J. (1991), Optimum data weighting and error calibration for estimation of gravitational parameters, *Bull. Geod.*, *65*, 44–52, doi:10.1007/BF00806341.

Lerch, F. J., et al. (1994), Geopotential models from satellite tracking, altimeter, and surface gravity data: GEM-T3 and GEM-T3S, *J. Geophys. Res.*, *93*, 6169–6215.

Mazarico, E., G. A. Neumann, D. D. Rowlands, and D. E. Smith (2010), Geodetic constraints from multi-beam altimeter crossovers, *J. Geodesy*, doi:10.1007/s00190-010-03791, in press.

McCarthy, J. (2008), *SOLVE Operations Manual*, SGT Inc., Greenbelt, Md.

Muller, P. M., and W. L. Sjogren (1968), Mascons: Lunar mass concentrations, *Science*, *161*, 680–684, doi:10.1126/science.161.3842.680.

Namiki, N., et al. (2009), Farside gravity field of the Moon from four-way Doppler measurements of SELENE (Kaguya), *Science*, *323*, 900–905, doi:10.1126/science.1168029.

Neumann, G. A., M. T. Zuber, D. E. Smith, and F. G. Lemoine (1996), The lunar crust: Global structure and signature of major basins, *J. Geophys. Res.*, *101*, 16,841–16,863, doi:10.1029/96JE01246.

Pavlis, D. E., S. G. Poulose, and J. J. McCarthy (2006), *GEODYN Operations Manual*, SGT Inc., Greenbelt, Md.

Ray, R. (1999), A global ocean tide model from TOPEX/Poseidon Satellite altimetry: GOT99.2, *Rep. NASA TM-1999–209478*, 66 pp., NASA Goddard Space Flight Cent., Greenbelt, Md.

Rowlands, D. D., F. G. Lemoine, D. S. Chinn, and S. B. Luthcke (2009), A simulation study of multi-beam altimetry for lunar reconnaissance orbiter and other planetary missions, *J. Geod.*, *83*, 709–721, doi:10.1007/s00190-008-0285-y.

Seidelmann, P. K., et al. (2002), Report of the IAU/IAG Working Group on cartographic coordinates and rotational elements of the planets and satellites: 2000, *Celestial Mech. Dyn. Astron.*, *82*, 83–111, doi:10.1023/A:1013939327465.

Smith, D. E., M. T. Zuber, G. A. Neumann, and F. G. Lemoine (1997), Topography of the Moon from the Clementine LIDAR, *J. Geophys. Res.*, *102*, 1591–1611, doi:10.1029/96JE02940.

Smith, D. E., et al. (2009), The Lunar Orbiter laser altimeter investigation on the lunar reconnaissance orbiter mission, *Space Sci. Rev.*, *150*, 209–241, doi:10.1007/s11214-009-9512-y.

Standish, E. M., X. X. Newhall, J.G. Williams, and W. F. Folkner (1995), JPL planetary and lunar ephemerides, *Rep. DE403/LE403, IOM 314.10–127*, Jet Propul. Lab., Pasadena, Calif.

Tapley, B., B. Schutz, and G. H. Born (2004), *Statistical Orbit Determination*, Elsevier, New York.

Williams, J. G., X. X. Newhall, and J. O. Dickey (1987), Lunar gravitational harmonics and reflector coordinates, in *Proceedings of the International Symposium on Figure and Dynamics of the Earth, Moon and Planets*, edited by P. Holota, pp. 643–648, Astron. Inst. of the Czech. Acad. of Sci., Prague.

Williams, J. G., D. H. Boggs, and W. M. Folkner (2008), DE421 lunar orbit, physical librations, and surface coordinates, *Rep. IOM 335-JW, DB,WF-20080314-001*, Jet Propul. Lab., Pasadena, Calif.

Zuber, M. T., D. E. Smith, L. Alkalai, D. H. Lehman, M. M. Watkins, and the GRAIL Team (2008), Outstanding questions on the internal structure and thermal evolution of the Moon and future prospects from the GRAIL mission, paper presented at the Lunar and Planetary Science Conference, Lunar and Planet. Inst., Houston, Tex

S.-C. Han, F. G. Lemoine, E. Mazarico, and D. E. Smith, NASA Goddard Space Flight Center, B34 W271, Greenbelt, MD 20771, USA. (erwan.m.mazarico@nasa.gov)